Rock-and-Walk Manipulation: Object Locomotion by Passive Rolling Dynamics and Periodic Active Control

Abdullah Nazir, Pu Xu, and Jungwon Seo, *Member, IEEE*

***Abstract*—This study presents the method of robotic *rock-and-walk* manipulation for dynamic, nonprehensile object locomotion. The object, which is in contact with an environmental surface, is basically manipulated to rock from side to side about the contact point periodically by the robot system. In the meantime, the passive dynamics due to gravity enables the object to roll along a zigzag path that leads to a forward walk. Rock-and-walk is a special-purpose method that enables the transport of a certain class of objects, which are too large, heavy to apply other primary methods such as grasping- or pushing-based operations. Our work is motivated by an interesting question in archaeology, how the giant statues of Easter Island (known as "moai") were transported several hundred years ago, and a recent demonstration performed by archaeologists that it is possible to walk the statue by periodic rocking. We present a detailed study of the dynamics, kinematics, and mechanics of the object-robot-environment system, and devise a feedback control strategy for rock-and-walk gaiting through the effective regulation of the object's energy and posture. An extensive set of experiments demonstrate the viability and practicality of our approach in diverse settings: Caging-based single-robot manipulation and cable-driven dual-robot manipulation using manipulator arms and aerial robots.**

***Index Terms*—Aerial manipulation, dynamics, mobile manipulation, passive walking, robust control of robotic systems.**

I. Introduction

EASTER island is the home of the well-known giant rock statues called "moai." It is known that there are more than 900 moai rock statues currently existing on the island and some of them approximately measure up to 10 m in height and 80 metric tons in weight. Historical evidence shows that the large, heavy statues were transported distances as far as 18 km across the island several hundred years ago. An interesting question in archaeology is how the moai statues, which must be extremely demanding to transport, were moved at that time [1]. Fig. 1(a) (from [1]) describes one viable answer to the question. The figure shows a replica of the statue with three ropes tied around the head, along with three groups of people interacting with the statue through the ropes. They demonstrated that it would be possible to "walk" the statue forward by repeatedly rocking it sideways, while its bottom edge is in rolling contact with the ground.[1]

Motivated by the way the statue was manipulated in Fig. 1(a), in this study we present a novel robotic dynamic manipulation method for object locomotion, which we call *rock-and-walk*

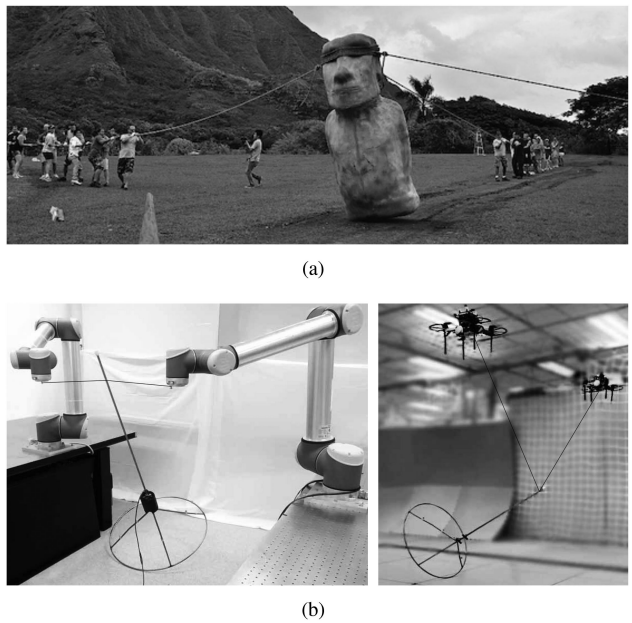

(a)

(b)

Fig. 1. (a) Walking a 3-m-tall, 4.35-tonne moai-replica with teams of experimenters handling three ropes. This figure is adopted from [1] with permission. (b) Our experiment setting for rock-and-walk manipulation featuring robot arms (left) and aerial robots (right) handling a cone-shaped object.

Manuscript received 16 August 2021; revised 6 December 2021; accepted 22 December 2021. Date of publication 21 January 2022; date of current version 8 August 2022. This work was supported by the Hong Kong Research Grants Council under Grant 26209319. This article was recommended for publication by Associate Editor Huichan Zhao and Editor Mark Yim upon evaluation of the reviewers' comments. *(Corresponding author: Jungwon Seo.)*

The authors are with the Hong Kong University of Science and Technology, Clear Water Bay, Hong Kong (e-mail: sanazir@connect.ust.hk; pxuaf@connect.ust.hk; junseo@ust.hk).

This article has supplementary downloadable multimedia material available at https://ieeexplore.ieee.org provided by the authors. This includes a video. The supplemental video in mp4 format can be played with any known players (in particular, it can be played with QuickTime Player version 10.4). Attachment filename: video_supplement.mp4 (36.9 MB) This video begins with showing the mechanical behavior of the object model. The video then shows our rock-and-walk technique for dynamic object transport implemented in diverse robotic settings: 1) Caging-based single-arm, 2) caging-based single-quadrotor, 3) cable-driven dual-arm, and 4) cable-driven dual-quadrotor.

This article has supplementary material provided by the authors and color versions of one or more figures available at https://doi.org/10.1109/TRO.2021.3140147.

Digital Object Identifier 10.1109/TRO.2021.3140147

[1] Video available here: https://www.youtube.com/watch?v=J5YR0uqPAI8

manipulation. In our robotic scenarios [Fig. 1(b)], the object to transport is driven by both its natural dynamics under gravity and the robot system. While the object, subjected to gravity, oscillates sideways around a point of stable equilibrium, the robot system is controlled to regulate the mechanical energy of the object and to move the object forward by changing its heading direction on the support surface through periodical nonprehensile interactions by means of, for example, cables, as shown in Fig. 1(b). Therefore, rock-and-walk manipulation enables dynamic object transport through the collaboration between the robot system and the environment. Following a formal problem description in Section III that also touches on the duality between manipulation and locomotion that can be seen in this transport method, Section IV presents a detailed analysis of the dynamics and kinematics with a representative object model. In Section V, a control strategy for successful rock-and-walk manipulation is presented; our controllers enable energy-sustainable rock-and-walk gaiting by periodically regulating the energy and the posture of an object. After a discussion of the stability and robustness of the method in Section VI, in Section VII we present a range of implementation scenarios using robot arms and aerial robots, as shown in Fig. 1(b), a set of experiments to verify the viability of our technical approach, and a discussion of performance and the range of application.

Our rock-and-walk manipulation makes it possible to transport objects by leveraging interaction with the environment and underactuated control. Therefore, the object can be handled in a nonprehensile manner, without firm grasping, and the robot only needs to periodically inject the amount of energy dissipated while the object interacts with the environment. This makes rock-and-walk applicable to objects that are too heavy or bulky to apply more straightforward and conventional methods such as grasp-lift-and-carry or pushing manipulation. However, rock-and-walk may need to be considered to be a special measure, rather than a primary mode of object transport, because the object needs to have certain features as can be observed in the moai statue.

A preliminary version of the presented study has appeared in [2]. We here provide a new problem description (Section III), a more rigorous dynamics formulation (Section IV-A), and a new analysis of the mechanics of object-robot-environment interaction (Section V-A). Based on these, our new feedback control strategy, elaborated and evaluated in Section V-B and Section V-C, leads to the effective regulation of the energy and the posture of the object, and, thus, enables rock-and-walk manipulation. The stability and robustness of rock-and-walk is also added in Section VI. Finally, we present more extensive rock-and-walk demonstrations in Section VII using a wider range of robot platforms, including a two-armed manipulator and aerial robots, on various terrain conditions, along with a new discussion of performance and the range of application.

II. Related Work

This section reviews related work on how robots have been used for dynamic and quasistatic manipulation, classified according to the model of mechanics, and how object manipulation techniques have been developed through caging-based and cable-driven approaches.

A. Dynamic Manipulation and Locomotion

The presented work is concerned with dynamic manipulation, in which the dynamics of the object to be handled is taken into account. Early examples of dynamic manipulation can be seen in part reorientation through tray tilting [3] and robotic juggling [4]. In [5], the control and planning of planar dynamic manipulation were addressed, and various dynamic tasks were demonstrated using a simple robot system. Low-dimensional model systems such as the acrobot, the pendubot, or the cart-pole have proven useful for inspiring solutions to more complex manipulation problems, as can be seen in [6] addressing cooperative dynamic manipulation by swinging. Recently, dynamic manipulation capabilities have been demonstrated in the tasks of in-hand repositioning [7], learning-based pick and throw [8], and robust manipulation using underactuated robot platforms [9].

Considering the duality between manipulation and locomotion (more discussion in Section III-A), our work is also relevant to passive dynamic locomotion. A modular loop robot presented in [10] was able to accelerate forward by means of the passive falling dynamics that is maintained by continuously reconfiguring itself to adjust the position of its center of mass. A method for legless locomotion was studied in [11], wherein a robot moves itself by inducing controlled body oscillations driven by coordinated leg motion. A seminal study presented in [12] introduces passive walking as a natural dynamic process that can be driven only by gravity with no active control. This passive dynamic walking approach has been extended in many directions as exemplified in the following. The authors in [13] showed that a representative two-legged model, which is statically unstable, can have stable limit-cycle walking motions. In [14], an efficient three-dimensional bipedal passive walker that is capable of knee flexion was presented. The control of a simple three-dimensional passive dynamic walker on a flat terrain was studied in [15]. A series of gravity-powered passive hopper mechanisms were presented in [16].

B. Object Transport Through Quasistatic Manipulation

Robotic quasistatic manipulation, wherein inertial forces are regarded as insignificant, is generally considered to be maturer than dynamic manipulation capabilities [17]. A wide range of quasistatic techniques are applicable to object transport. For example, there is a vast amount of literature on robotic grasping and fixturing (see [18] and references therein), one of the most fundamental problems in manipulation, which leads to conventional grasp-lift-and-carry approaches to object transport. Variants of the problem of grasping have been studied in picking or scooping manipulation [19]–[21]. Quasistatic pushing is another well-studied mode of object transport. The fundamental model of planar pushing presented in [22] has been extended to stable pushing using an edge-to-edge contact [23], in-hand manipulation planning [24], data-driven pushing [25], among others. Rolling manipulation can be an effective way of transport for

those objects that have a curved face [26] or a circular edge [27]. Pivoting manipulation [28]–[30] lends itself to moving prismatic objects through repeated rotation about one of the vertices in contact with a support surface.

C. Caging-Based and Cable-Driven Manipulation

Our object transport method will be realized through nonprehensile manipulation, referring to "manipulation without grasping" [5], [31]. Specifically, we will apply a caging-based and a cable-driven approach to nonprehensile manipulation.

Robotic caging is concerned with how to bound an object's mobility by arranging robotic fingers/effectors, which are regarded as obstacles in the configuration space of the object. A recent survey of caging is presented in [32]. A cage may still allow some free space for the object to move around, but caging can mitigate some challenging issues encountered in prehensile manipulation such as contact modeling and grasp force optimization. Finding cages is a well-studied computation problem; see [33] for a recent example and the references therein for previous approaches. Caging has been applied to robustifying robotic grasping and manipulation. Early examples include vision-based error-tolerant planar grasping, presented in [34]. The relationship between caging and grasping was discussed in [35]: A cage can be a precondition for an equilibrium grasp. In [36], whole-arm grasping was addressed through caging with the end-effectors that have curved contact surfaces. Whole-hand dexterous manipulation based on caging and compliance was discussed in [37]. Caging has also found application in cooperative object transport [38], [39].

Cables have long been used as effective robotic end-effectors due to their advantages in large motion ranges, small footprints, and low inertia. Successful examples include the Skycam system, which is used to cover live sporting events. An early study of cable-driven manipulation can be seen in [40], wherein a wire-actuated manipulator was presented that is capable of dexterous quasistatic pose control for a payload. Dynamic cable-driven manipulation has received attention as a way to extend the limited workspace in quasistatic manipulation; examples can be seen in casting manipulation [41] and dynamic point-to-point motion control [42]. A growing body of recent studies address cable-driven aerial manipulation in a range of scenarios: For example, quasistatic payload transport [43], dynamic transport of a cable-suspended load [44], and cooperative transport through distributed optimization [45].

III. Problem Description

This section states our research problem and introduces a model system to be examined.

A. Problem Statement

In cases of moving objects that are too heavy or bulky to be grasped or lifted, the moai example in Fig. 1(a) shows that it is workable to concatenate small dynamic rolling maneuvers to generate net forward motion. Our goal is to confirm the hypothesis that this dynamic rolling gait can be realized with a general object model through the coordinated interaction between an object, a robotic system, and their environment. It is envisioned that the robot, like the experimenters in Fig. 1(a), will provide necessary mobility for the object with no internal mobility to take subsequent steps in a nonprehensile manner, while the object is in rolling contact with the ground. As a result, the object is expected to "walk" like the moai statue. The envisioned behavior can thus be considered as an additional example showing the well-known duality between locomotion and manipulation observed in both living and artificial systems,[2] which is accounted for by the observation that the two important capabilities share the same fundamental mechanics of frictional contact.

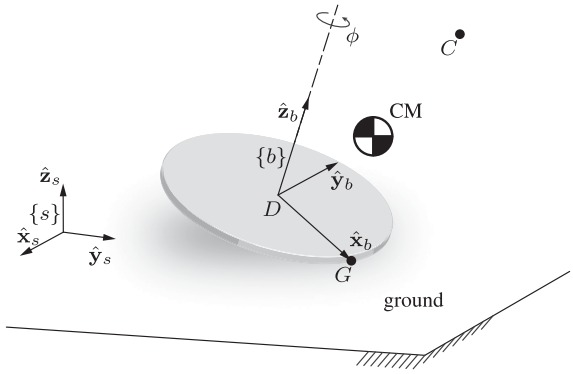

Fig. 2. Object model: The combination of a rigid disk and a point denoted C. The disk is in contact with a flat, rigid ground surface at G. The disk is not necessarily perpendicular to the surface. The mass center of the model, denoted CM, is located off the plane of the disk.

B. Model System

See Fig. 2 illustrating our object model to be investigated. It is composed of a rigid disk and a point at C situated out of the plane of the disk. The disk and the point C are assumed to be connected rigidly and behave essentially like a single rigid body. Accordingly, the disk-point pair can also be considered to be an oblique circular cone. The mass of the object model is assumed to be concentrated at the center of mass, located off the disk. These model the characteristics of the moai statues [1]: Curved bottom edge and eccentric mass distribution. The role of a robot system in this study is to take control of the point C, at the apex of the cone: The disk-point object model is subjected to the holonomic constraint that the motion of C is fully controlled by the robot. The point C will thus be called the *control point*. The object model is also subjected to the nonholonomic constraint that it rolls without slipping on the contact point G between the disk and a flat, rigid ground surface. The object is thus manipulated in an underactuated manner: No control torques can be imparted about the axis of $\overline{CG}$. Note, the plane of the disk is not necessarily normal to the ground. Overall, the two

[2]The workshop entitled, *"Locomotion and Manipulation, Why the Great Divide,"* (held in Arlington, VA, USA in Apr 2015) provides more information. The workshop materials are available online as of Dec 2021.

constraints at C and G abstract how the object interacts with its environment in the motivating example of moai.

Two reference frames are shown in Fig. 2. $\{s\}$ denotes the space frame, which is stationary and inertial: Its $\hat{\mathbf{z}}_s$-axis is perpendicular to the ground surface and gravity acts in the negative $\hat{\mathbf{z}}_s$-direction. The object frame $\{b\}$ is attached to D (the center of the disk) and moves with it such that its $\hat{\mathbf{x}}_b$-axis always points toward G, $\hat{\mathbf{y}}_b$-axis is parallel to the ground, and $\hat{\mathbf{z}}_b$-axis is coincident with the axis of the disk. These frames are established in the same manner as the example of the disk "rolling in a wobbly manner" [46] or the "falling rolling disk" [47]. These refer to a disk that rolls without slipping on the ground such that its axis is not necessarily parallel to the ground. Our model in Fig. 2 builds on them by allowing the center of mass to be located off the geometric center of the disk and also off the plane of the disk, and by adding the constraint at the control point C.

The configuration space of the object model is expressed by the five-dimensional space $\mathbb{R}^2 \times SO(3)$, for its configuration can be described by the position on the ground plane $\mathbb{R}^2$ and spatial orientation $SO(3)$. One way to parametrize the configuration space is to use the generalized coordinates $\mathbf{q}$

$$\mathbf{q} = (q_1, q_2, q_3, q_4, q_5) = (x_D, y_D, \psi, \theta, \phi) \tag{1}$$

(x_D, y_D) is the position of D in the $\hat{\mathbf{x}}_s\hat{\mathbf{y}}_s$-plane. ψ, θ, and ϕ are the Euler angles that represent the orientation of the object: The precession angle ψ, a rotation about the $\hat{\mathbf{z}}_s$-axis; the nutation angle θ, a rotation about the $\hat{\mathbf{y}}_b$-axis; and the spin angle ϕ, a rotation about the $\hat{\mathbf{z}}_b$-axis. We assume that at the spin value $\phi = 0$ (and, thus, π), the center of mass and C are on the $\hat{\mathbf{x}}_b\hat{\mathbf{z}}_b$-plane, which can thus be considered to be the plane of symmetry of the oblique-cone-shaped model when $\phi = 0$ or π.

IV. Passive Dynamics and Kinematics

This section investigates the passive dynamics and kinematics of the model system in Fig. 2.

A. Passive Dynamics of the Object Model

The equation of motion for the object model shown in Fig. 2 can be derived by the Lagrangian dynamics formulation. Let the Lagrangian $\mathcal{L} = T - V$, where T and V denote the kinetic and the potential energy, respectively. Then the dynamics equation is given as

$$\frac{d}{dt}\left(\frac{\partial \mathcal{L}}{\partial \dot{\mathbf{q}}}\right) - \frac{\partial \mathcal{L}}{\partial \mathbf{q}} = \mathbf{A}^T(\mathbf{q})\boldsymbol{\lambda} + \boldsymbol{\zeta} \tag{2}$$

representing the collection of five scalar equations, one for each generalized coordinate. For now, we are mainly concerned with the passive dynamics of the object, in which the control point C is held fixed by the robot. Therefore, the external force $\boldsymbol{\zeta}$ is set to be zero. $\mathbf{A}(\mathbf{q}) \in \mathbb{R}^{4\times 5}$ represents the coefficients of the Pfaffian constraints $\mathbf{A}(\mathbf{q})\dot{\mathbf{q}} = \mathbf{0}$ imposing zero velocities at C and G, due to the nonholonomic and holonomic constraints. See Appendix for T, V, and $\mathbf{A}(\mathbf{q})$ presented in full. $\boldsymbol{\lambda}$ denotes the vector of the Lagrange multipliers, the reaction forces to keep these constraints active. The constraints will reduce the degrees-of-freedom (DOF) of the object model to one: The five-dimensional generalized coordinates $\mathbf{q}$ with four constraints. The resulting one-DOF motion can instantaneously be described by the rotation about the axis of $\overline{CG}$ since C and G are fixed in place. When $\phi = 0$ or π, the object can be in static equilibrium because the moment of gravity about $\overline{CG}$ vanishes. We further assume that the configuration with $\phi = 0$ ($\phi = \pi$) is in stable (unstable) equilibrium in which the center of mass is at its lowest (highest). Unless $\phi = 0$ or π, the moments of gravity cannot be balanced and it will accelerate the object back toward the stable equilibrium point $\phi = 0$, while the object rolls without slipping. This will cause the object to oscillate about the configuration $\phi = 0$, like a one-DOF, simple gravity pendulum.

Computationally, the following system of differential equations, with nine unknowns (the five generalized coordinates and the four Lagrange multipliers), formulated according to the *augmented method* [46], is solved for the constrained dynamics of the object model

$$\begin{bmatrix} -\mathbf{A} & 0 \\ \mathbf{M} & -\mathbf{A}^T \end{bmatrix} \begin{bmatrix} \ddot{\mathbf{q}} \\ \boldsymbol{\lambda} \end{bmatrix} = \begin{bmatrix} \dot{\mathbf{A}}\dot{\mathbf{q}} \\ -\mathbf{h} \end{bmatrix} \tag{3}$$

which is obtained by putting together the time derivative of the constraints

$$\frac{d}{dt}(\mathbf{A}(\mathbf{q})\dot{\mathbf{q}}) = \mathbf{A}(\mathbf{q})\ddot{\mathbf{q}} + \dot{\mathbf{A}}(\mathbf{q})\dot{\mathbf{q}} = \mathbf{0} \tag{4}$$

and the equation of motion expressed in the standard matrix form

$$\mathbf{M}(\mathbf{q})\ddot{\mathbf{q}} + \mathbf{h}(\mathbf{q}, \dot{\mathbf{q}}) - \mathbf{A}^T(\mathbf{q})\boldsymbol{\lambda} = \mathbf{0} \tag{5}$$

where $\mathbf{M}(\mathbf{q})$ is the mass matrix and $\mathbf{h}(\mathbf{q}, \dot{\mathbf{q}})$ lump other terms together. Fig. 3(a) instances a solution to (3). It confirms that the object oscillates by rolling from side to side about the equilibrium point $\phi = 0$.

Our model produces the fastest dynamics achievable, by having the whole mass concentrated at the center of mass. Distributed mass would increase the radius of oscillation and in turn the period of oscillation by dislocating the center of oscillation further from the center of mass. This is confirmed in Fig. 3(b), presenting a comparison of the periods of oscillation computed by our dynamic model at various nutation values with those measured in experiments performed with actual objects of the same dimension. The discrepancy may also have been caused by damping induced by rolling friction, which is ignored in our dynamics formulation. Because the oscillation of the object is caused by the component of the moment of gravity around the axis of $\overline{CG}$, the cadences are expected not to be heavily affected by $\overline{CG}$'s orientation (i.e., nutation θ). This is also confirmed by the plot.

B. Contact Kinematics of the Constrained Object Model

Given the control point C fixed, the set of all the possible positions of the ground contact point G can be represented as an annulus on the flat ground surface [Fig. 4(a)] because of the rotational symmetry of the object's configurations about the axis of $\overline{CC'}$, where C' is the foot of perpendicular of C to the ground. The size and the aspect ratio of the annulus are determined by the geometry of the object and the height of C. When $\phi = 0$ ($\phi =$

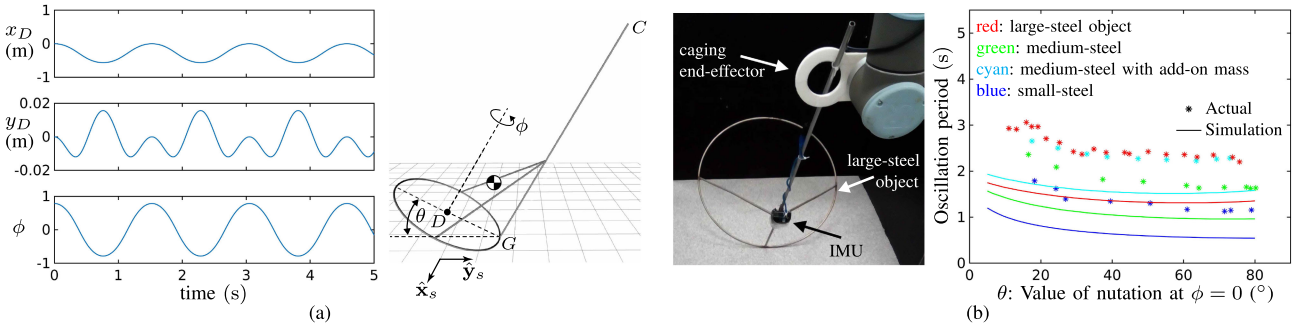

Fig. 3. (a) Computed passive dynamics of the object modeled as an oblique cone that has a circular base and a straight column attached to it. The plots, showing the time history of the generalized coordinates x_D, y_D, and ϕ, exemplify one of the simulations reported in (b) performed with the large-steel object. (b) Comparison of oscillation periods in simulations and experiments. In the experiments, the object is held by a torus-shaped end-effector placed at C and the period is measured using an inertia measurement unit (IMU). Fig. 8 has more details of the test objects, distinguished by colors in the plot.

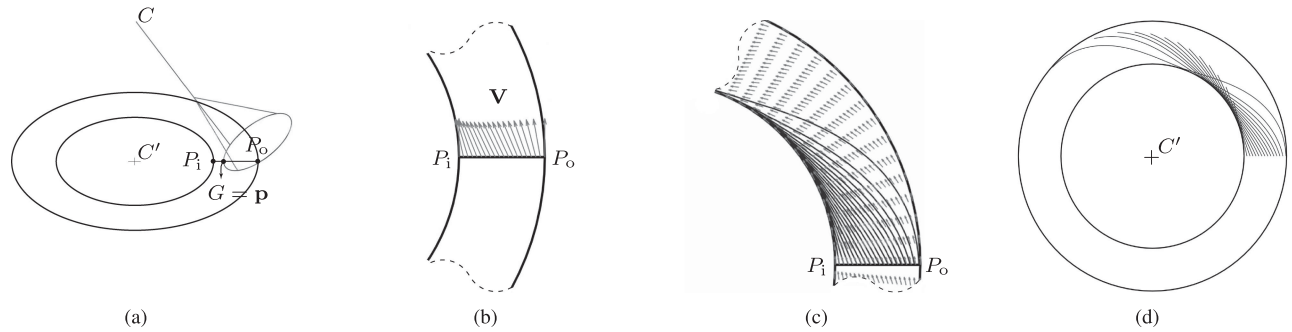

Fig. 4. (a) Annulus represents the set of all the feasible positions of G on the flat support surface, given C fixed. C' is the foot of perpendicular of C to the surface. $\overline{P_\mathrm{i}P_\mathrm{o}}$ is a line segment normal to the circles. (b) For each $\mathbf{p} \in \overline{P_\mathrm{i}P_\mathrm{o}}$, $\mathbf{V}(\mathbf{p})$, the heading direction of the base disk of the cone-shaped object shown in (a), is computed. (c) Vector field on $\overline{P_\mathrm{i}P_\mathrm{o}}$ is parallel-transported to fill the entire annulus, and the integral curves are obtained. (d) Integral curves describing the local motion paths around the points on the inner circle.

π), G is right on the inner (outer) circle of the annulus, where the object model can be in stable (unstable) equilibrium. While the object oscillates about the point $\phi = 0$ as it rolls without slipping, G will move along a one-dimensional curve on the annulus because the object moves with one DOF.

The curve representing the path traced by G can be found by solving for the holonomic and nonholonomic constraints, in other words, by integrating the vector field of the heading directions of the base disk established on the annulus. First, consider a line segment $\overline{P_\mathrm{i}P_\mathrm{o}}$ traversing the annulus between the inner and the outer circle, and perpendicular to these circles [Fig. 4(a)]. Second, at each point on the line segment, denoted $\mathbf{p} \in \overline{P_\mathrm{i}P_\mathrm{o}}$, a unit vector $\mathbf{V}(\mathbf{p})$ is assigned such that it represents the direction of the heading of the base disk when G coincides with $\mathbf{p}$ [Fig. 4(b)]. The direction can be found by intersecting the plane of the ground surface and the plane of the base of the object. Specifically, it can be represented using the vector cross product

$$\mathbf{V}(\mathbf{p}) = \frac{\hat{\mathbf{b}}_s \times \hat{\mathbf{g}}_s}{||\hat{\mathbf{b}}_s \times \hat{\mathbf{g}}_s||} \tag{6}$$

where $\hat{\mathbf{b}}_s$ ($\hat{\mathbf{g}}_s$) denotes the unit normal vector to the base (ground), expressed with respect to the space frame $\{s\}$, when G coincides with $\mathbf{p}$. $\hat{\mathbf{g}}_s$ is a constant vector relative to the space frame $\{s\}$. $\hat{\mathbf{b}}_s$ can be found by multiplying $\hat{\mathbf{b}}_b$ (the vector $\hat{\mathbf{b}}$ relative to the body frame $\{b\}$ fixed to the object, which is a constant vector) and the rotation matrix between $\{b\}$ and $\{s\}$, which is uniquely determined by 1) the orientation of the line connecting C and $\mathbf{p}$, which will determine two of the three unknowns of the rotation matrix, and 2) the tangency of the base to the ground surface (the remaining, third unknown). Third, considering the rotational symmetry of the system, the vector field on $\overline{P_\mathrm{i}P_\mathrm{o}}$ is parallel-transported along the concentric arcs to fill the annulus, and the paths traced by G are obtained by integrating the vector field over the annulus [Fig. 4(c)]. The existence of the integral curves is confirmed by considering that the directions of the unit vectors on $\overline{P_\mathrm{i}P_\mathrm{o}}$ change smoothly [from (6)] and the parallel transport along the concentric arcs is also a differentiable operation.

In addition to the "counterclockwise" vector field shown in Fig. 4(c), along which the object will roll counterclockwise about C', the clockwise vector field can also be constructed by flipping the vector field. The integral curves of these two vector fields are connected smoothly at the points on the inner circle. Fig. 4(d) shows some of these connected integral curves that are tangent to the inner circle. They now fully depict the motion paths of the object driven by the constrained dynamics when G

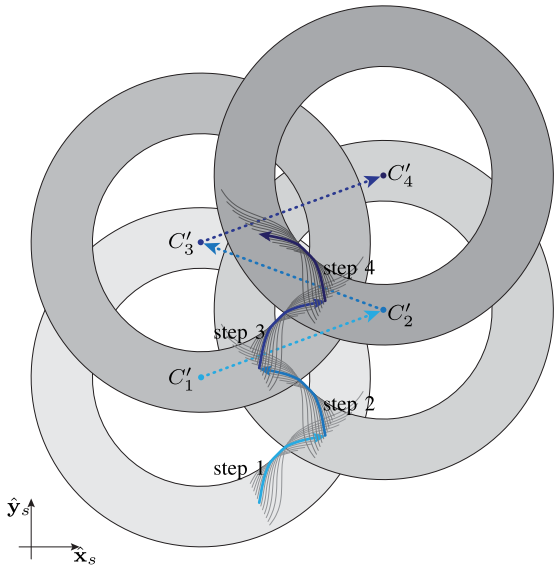

Fig. 5. Concatenating steps, each of which is shown as a solid arrow curve representing an integral curve inside the annulus, as shown in Fig. 4(d). G will move along the piecewise smooth trajectory, which darkens as it proceeds forward in the positive $\hat{\mathbf{y}}_s$-direction.

is near the inner circle, on which stable equilibrium is obtained. Unless the object slides on the surface, G cannot move across to different integral curves.

C. Availability of the Passive Oscillatory Dynamics

Whether the passive dynamic oscillation will happen or not depends on the geometric and mass properties of an object. In essence, it is necessary for the object to have a low center of mass and a bottom edge of sufficiently small curvature, analogous to roly poly toys. The discussion of kinematics in Section IV-B provides a way to test the availability of the passive dynamics. First, approximate a given object using the model in Fig. 2. Second, solve for the integral curve. Finally, verify the object's center of mass is at its lowest height at the point where $\phi = 0$. If so, the oscillatory dynamics will occur.

V. Active Gait Control for Rock and Walk

One way to spread the passive oscillatory motions out to produce net displacement of the object is to periodically steer the object, inspired by Lie bracket motions [17] (see [11] for an example from robotic locomotion). Fig. 5 presents a kinematic scheme illustrating this idea: The four smooth integral curves, each of which represents an individual rolling motion described in Fig. 4(d) and will be denoted a "step," are connected sequentially into a zigzag path for G. At the end of each step i, the control point C is relocated to steer the object such that its foot of perpendicular on the ground surface C' moves from C'_i to C'_{i+1}. This will eventually enable the object to walk in the positive $\hat{\mathbf{y}}_s$-direction, while it rocks from side to side: *Rock-and-walk* manipulation. This kinematic blueprint also implies a way to realize the rock-and-walk gaiting: Combine continuous passive dynamic oscillation and discrete, periodic active steering control. Unlike many other locomotion approaches, whereby such "yawing" (that is, rotation about an axis normal to the ground) is suppressed, our rock-and-walk manipulation can take advantage of it.

In this section, we first investigate how the object model mechanically interacts with its surroundings and then discuss a strategy for energy-sustainable rock-and-walk control based on the mechanics model.

A. Mechanics of Object-Robot-Environment Interaction

We begin by examining how the external forces applied to the control point C, denoted $\mathbf{f}^C$, affect the behavior of the object model near the stable equilibrium configuration $\phi = 0$. See Fig. 6. We focus on the forces that are mainly exerted sideways, i.e., in the direction that is tangential to the base disk at G. Specifically, we set up the frame $\{g\}$ at G such that its y-axis is tangential to the base at G and its z-axis is normal to the ground. We then consider the case $|f_y| \gg |f_{x,z}|$, where $\mathbf{f}_g^C = [f_x \ f_y \ f_z]^T$ denotes $\mathbf{f}^C$ expressed in the $\{g\}$ frame.

In response to $\mathbf{f}^C$, the object exhibits two qualitatively different types of behavior (refer to the video attachment) depending on the value of nutation θ, the angle between the ground surface and the bottom face of the object, considering the moment of $\mathbf{f}^C$ about G. The following paragraphs elaborate these.

1) Small Nutation: In the case of a nearly upright configuration with a relatively small nutation value θ, we consider the motion of the object on the $\hat{\mathbf{y}}_g\hat{\mathbf{z}}_g$-plane, as depicted in Fig. 6(a) since the x-component of the moment of $\mathbf{f}^C$ about G will dominate, with respect to the frame $\{g\}$. We here show that $\mathbf{f}^C$ will tilt the object, while it rolls on the ground contact G (in other words, G remains fixed), given sufficiently large friction there.

a) G fixed: Suppose that G is fixed. Then the composite wrench cone spanned by the contact wrenches exerted on the object at G and C is represented in Fig. 6(a) as the shaded regions labeled "$-$" or "$+$" that are formed by the edges of the friction cone at G (denoted $\mathbf{f}^{G_{1,2}}$) and the line of $\mathbf{f}^C$, according to the method of *moment labeling* [17]. The "$-$" ("$+$") label indicates that if the moment of an external force acting on the object about an arbitrary point in that region is positive (negative), then that external force can be counterbalanced. In a quasistatic setting, the force of gravity $m\mathbf{g}$ shown in Fig. 6(a) can thus be balanced. Force balance can also be maintained in the presence of other forces as long as their resultant does not intersect the shaded regions. For example, in a dynamic setting in which the center of mass accelerates to the left (in the negative $\hat{\mathbf{y}}_g$-direction) or right, Fig. 6(a) accordingly shows the maximum possible lateral accelerations, denoted $\mathbf{a}_{\max}^{\text{left}}$ and $\mathbf{a}_{\max}^{\text{right}}$, considering the lines connecting the center of mass and the vertices of the shaded regions, each of which is represented as a convex polytope.

b) G nonfixed: If G is nonfixed, that is, sliding or breaking free, a similar analysis shows that it is impossible to counterbalance the external forces exerted on the center of mass, with the contact wrenches.

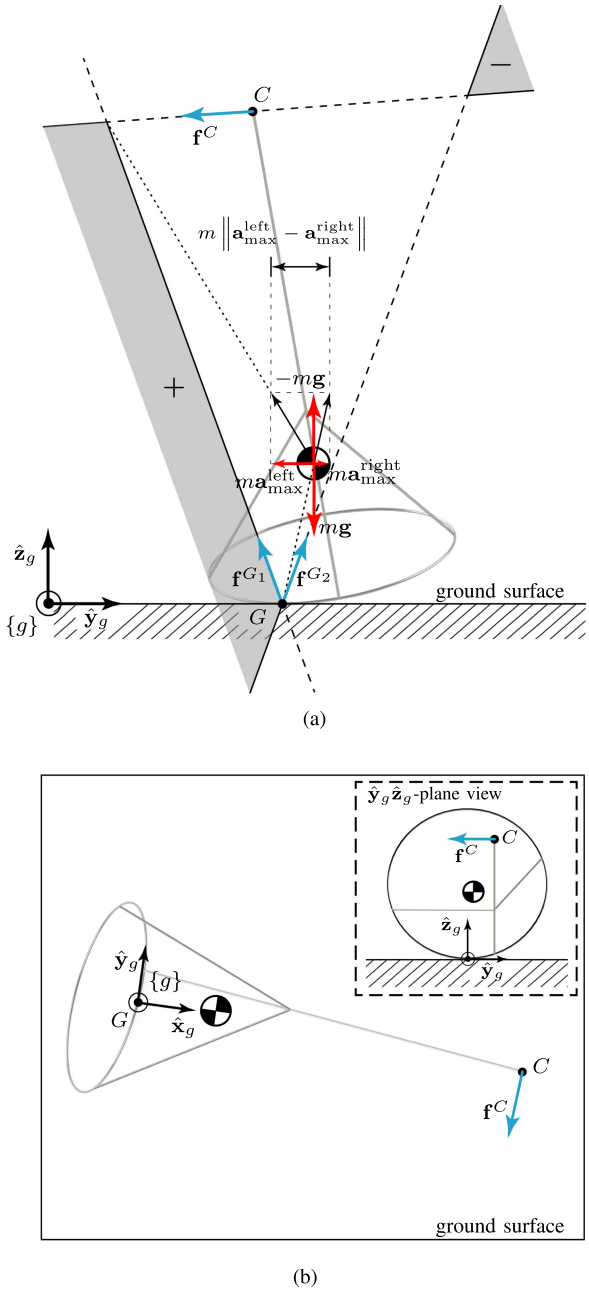

Fig. 6. Our oblique-circular-cone-shaped object model (featured in Figs. 3 and 4) at a configuration of (a) small (i.e., almost upright posture) and (b) large nutation θ. The model is presented on the plane normal to the ground in (a) and on the horizontal ground surface in (b). The origin of the frame $\{g\}$ is at G, but they are shown separately in (a) for less busy visualization.

In conclusion, a theoretically consistent solution to the motion of the object is sideways tilting by rolling on fixed G, whose location will evolve along the curved bottom edge of the object as it is being tilted.

2) Large Nutation: In the case of relatively large nutation [Fig. 6(b)], the z-component of the moment of $\mathbf{f}^C$ about G dominates. The resulting motion of the object can thus be investigated on the $\hat{\mathbf{x}}_g\hat{\mathbf{y}}_g$-plane, as shown in the figure. We apply the concept of the *limit surface* [17], which models the motion-force mapping in planar pushing. If we assume that the deformation at G, an isolated point of support, is negligible, the limit surface here is represented as an almost flat body in the three-dimensional wrench space related to the planar pushing on the $\hat{\mathbf{x}}_g\hat{\mathbf{y}}_g$-plane, since it is essentially unable for the object to exert moment loads about G. The thinness of the body is thus seen in a direction normal to the moment axis of the wrench space. Because the allowable twist of the object is normal to the limit surface, the almost flat limit surface gives rise to essentially the same motion, that is, rotation about the axis normal to the ground at G, given distinct load conditions. Therefore, $\mathbf{f}^C$ has no effect on the orientation of the object relative to the ground, except for differences accounted for by the rotation about the normal at G, in the case of a relatively large nutation value. Neither will the tilting of the object nor the relocation of G happen.

The analysis above matches well with what can be observed in actual practice, as can be seen in the video attachment.

B. Gait Control for Rock and Walk

To realize rock-and-walk gaiting as envisioned in Fig. 5, it is necessary to preserve the mechanical energy of the object, to be denoted $\mathcal{E}$, by compensating any loss as the object interacts with the ground, due to rolling friction at G for example. The tilting manipulation discussed in Section V-A1 is applicable to this task of energy pumping. While the object is being tilted sideways, as shown in Fig. 6(a), its curved bottom edge will be rolling on the ground surface. This will increase the amplitude of oscillation by moving the ground contact point G further away from the position of equilibrium. Therefore, the amount of tilting and the increase in the object's energy are positively correlated. More specifically, for small values of the spin ϕ near the stable equilibrium configuration, the change of $\mathcal{E}$ before and after a tilt, denoted $\tilde{\mathcal{E}}$, can be linearly proportional to the amount of the tilt u

$$u \propto \tilde{\mathcal{E}}. \tag{7}$$

This consideration, to be confirmed in Section V-C, motivates the formulation of our energy controller.

1) Energy Control: Our energy controller dictates the discrete-time periodic actions for regulating the object's mechanical energy $\mathcal{E}$. In essence, a tilt is performed at the end of each step, when the velocity of the object becomes zero, by moving the control point C in the $\hat{\mathbf{y}}_g$-direction such that G moves away from the equilibrium point and thus energy can be injected according to the dynamics of energy pumping in (7). As illustrated in Fig. 5, the directions of successive tilts should alternate left and right (i.e., in the negative and the positive $\hat{\mathbf{y}}_g$-direction), with respect to the heading direction of walking shown as the $\hat{\mathbf{y}}_s$-axis in the figure. The amount of the tilt at the end of step j, denoted $u[j]$, is given by the following feedforward plus linear feedback control law considering that the control objective is setpoint control at constant $\mathcal{E}$

$$u[j] = u_{\text{ff}}[j] - \left(K_{\text{P}}\mathcal{E}_{\text{e}} + K_{\text{I}}\sum \mathcal{E}_{\text{e}} + K_{\text{D}}\Delta\mathcal{E}_{\text{e}}\right) \tag{8}$$

where

1) $u_{\text{ff}}[j]$: Feedforward term

2) K_{P}, K_{I}, and K_{D}: Proportional, integral, and derivative control gains
3) $\mathcal{E}_{\mathrm{e}} = \mathcal{E}_{\mathrm{desired}} - \mathcal{E}$: The difference between $\mathcal{E}_{\mathrm{desired}}$, the desired value of $\mathcal{E}$ and its current value. It can be evaluated discretely, for example, once in each step. $\sum \mathcal{E}_{\mathrm{e}}$ and $\Delta\mathcal{E}_{\mathrm{e}}$ are then, respectively, interpreted as the sum and the difference of the discretely measured values.

Our energy setpoint controller is applicable to both initial transient swing-up and subsequent steady rock and walk. In the steady phase of a rock-and-walk gait, the amount of work to be pumped by the robot only needs to be sufficient to compensate for the energy dissipated, while the object rolls on the ground. The presented way of energy pumping through tilting manipulation makes it possible to swing up the underactuated object by taking advantage of the interaction with the environment. This is distinct from conventional approaches to swing-up control for other model systems such as the cart-pole [48] or the acrobot system [49].

2) Heading Direction Control: The control for the object's heading direction is achieved by taking advantage of the energy control described above. A tilt by relocating C according to (8) additionally results in the object's precession (in other words, yawing), a rotation about the $\hat{\mathbf{z}}_s$-axis that is normal to the ground, as described in Fig. 5. This makes it possible to steer the object to the right (left) by, for example, lessening or skipping the leftward (rightward) tilt maneuvers. Therefore, car-like planar reachability is attainable with the object.

3) Nutation Control: In order to take advantage of our energy pumping mechanism by tilting, which is also applicable to the heading direction control, it is critical to regulate the value of the nutation θ as discussed in Section V-A. This is performed periodically by adjusting θ whenever the object passes through the equilibrium point $\phi = 0$. At these instants, the object is rotated about the $\hat{\mathbf{y}}_g$-axis (Fig. 6), which is tangent to the base at G, by the robot holding the control point C in order to nullify the error between the current and the desired value of nutation. This action is also applied at the beginning of a gait, for tipping the object forward from an upright configuration, and at the end, for raising the object back upright again.

In summary, these controllers allow the robot to use the motion of the control point C as both a "cruise control" and a "steering wheel," by analogy with the car. We again note that, the controllers specify discrete and periodic actions. The energy (nutation) control is executed at the end of a step (in the middle of a step), while the object continuously oscillates by rolling passively.

C. Implementation of the Rock-and-Walk Controllers

All the control actions discussed in the previous subsection can be implemented using motion control for moving the control point C.

In the energy control, the geometric information encoded in the object's configuration $\mathbf{q}$ provides all the necessary input data. First, the direction of tilting, the $\hat{\mathbf{y}}_g$-direction, is dictated by $\mathbf{q}$ directly. Second, the value of the mechanical energy of the object $\mathcal{E}$, which is processed to determine the amount of tilting, is obtained by monitoring the value of the spin angle ϕ or the trace of G. The specific time scaling of the point-to-point motion path of C for a tilt is then performed by taking into account the maximum possible lateral accelerations, $\mathbf{a}_{\max}^{\mathrm{left}}$ and $\mathbf{a}_{\max}^{\mathrm{right}}$ presented in Fig. 6(a). The posture (heading and nutation) control actions are also parametrized using the same input data.

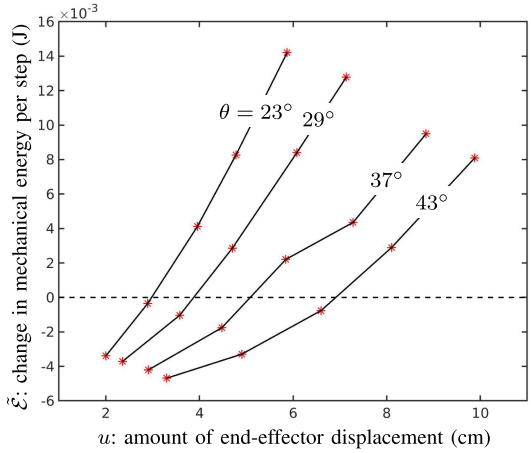

Fig. 7. Experiment results showing how tilting manipulation can pump up energy, for four different nominal values of the nutation θ, on a level ground surface. Each data point, denoted $*$, represents $\tilde{\mathcal{E}}$, the change of energy per step (here averaged over ten successive tilts), given a tilt of magnitude u which was arranged to complete in 0.6 s. Initially, the spinning amplitude of the object $\phi_{\max} \approx 30°$.

We verified the soundness of our controller implementation through a set of experiments. The experiment setting is the same as Fig. 3(b), using the end-effector for caging the object. We control the robot to move the end-effector according to the control laws such that the object walks forward along a straight line on a level surface. When the amount of tilting $u[j]$ [(8)] was fixed at a small value (at most 10 cm for the 1.5-m tall object) regardless of j, the suggested linear relationship between u and $\tilde{\mathcal{E}}$ [(7)] was confirmed as presented in Fig. 7. The results presented in Fig. 7 also support the analysis of the behavior of the object model in Section V-A, by showing that energy pumping by tilting becomes more effective when the nutation θ is smaller.

The linear plant dynamics in (7), more specifically affine dynamics as can be seen in Fig. 7, suggests that the error dynamics of the setpoint control in (8) is represented as a linear differential equation in which the control gains K_{P}, K_{I}, and K_{D} are incorporated as its coefficients. The control gains can then be determined to realize a desired error response. Lastly, the feedforward term $u_{\mathrm{ff}}[j]$ can be set as the value of u when $\tilde{\mathcal{E}} = 0$, considering the affine relationship shown in Fig. 7.

VI. Stability and Robustness of Rock and Walk

Bridging between the theoretical development up to this point and the experiments to follow, this section addresses the stability and robustness of rock-and-walk manipulation.

A. Stability

We first review the behavior of an object during a rock-and-walk gait and confirm that it remains stable. In the robotic locomotion literature (for example, see [50]), the terms "stability" and "balance" are used interchangeably. We thus discuss, specifically, the balancing of the object when the control point C is held firm; otherwise, the system is a decoupled combination of the robot and the rigid object, which is of no interest in this study. First, in the passive dynamic phase, the object is not statically balanced unless $\phi = 0$, the equilibrium point. However, the object is dynamically stable since it will always be accelerated toward the point. Second, during the active control actions, the object can also be kept stable on fixed G since the force resultant exerted at the center of mass can be balanced by the contact wrenches as analyzed in Fig. 6(a).

Since our rock-and-walk manipulation does not rely on a specific model of a robot system, the question of the stability of the robot is not as well posed as that of the object discussed above. That being said, it can be easier to stabilize the robot in rock-and-walk manipulation, because the robot only needs to bear a fraction of the weight of the object that stays in contact with the ground at G, compared with other modes of manipulation (e.g., grasp, lift, and carry) in which the robot needs to support the entire load. Specifically, the reaction force on the robot is obtained by adding the static force to leverage the object's weight with respect to G and the dynamic force due to the rotating unbalance—the center of mass of the object out of alignment with the axis $\overline{CG}$. As the weight of the object increases, the dynamic force is expected to become less significant, because the object does not exhibit fast dynamics (recall Fig. 3).

B. Robustness

The performance of rock and walk using our controllers is robust to bounded uncertainties and errors.

First, one way to quantify the robustness of the energy control is to consider

$$\left\|\mathbf{a}_{\max}^{\text{left}} - \mathbf{a}_{\max}^{\text{right}}\right\| \tag{9}$$

representing the range of the allowable lateral accelerations to keep the system balanced; see Fig. 6(a). Considering the geometry of the composite wrench cone shown in the figure, friction at G can make the value of (9) nonzero, and the value increases as the friction at G increases. Recall that the object's mass center is located right above G at the spin $\phi = 0$, on the $\hat{\mathbf{y}}_g\hat{\mathbf{z}}_g$-plane shown in Fig. 6(a). As ϕ increases, G becomes more separated horizontally from the mass center, and this can also increase the value of (9). Therefore, performing a tilt at the end of a step as suggested by our control strategy has the advantage of increased robustness. Another way to increase the value is to direct $\mathbf{f}^C$ toward a lower level. For example, recall the three scenarios in Fig. 1. Compared with our robotic cases in Fig. 1(b), $\mathbf{f}^C$ by the human experimenters in Fig. 1(a) is directed toward a lower position, to the ground. According to Fig. 6(a), $\mathbf{f}^C$ redirected downward will increase $\mathbf{a}_{\max}^{\text{left}}$, and, thus, the value of (9). In other words, our robotic rock-and-walk setting in Fig. 1(b), to be demonstrated in the next section, deals with a more challenging case (i.e., decreased robustness) than the motivating moai example.

Second, the other control action for adjusting the nutation θ changes the orientation of the axis $\overline{CG}$. The dynamics of the object remains robust to the reorientation: Qualitatively, the object keeps oscillating passively about $\overline{CG}$; quantitatively, the period of oscillation does not change dramatically [recall the analysis in Section IV-A and Fig. 3(b)].

VII. Experiments

This section presents our hardware and software implementation for rock-and-walk manipulation and reports a set of experiments along with a discussion of the results. See also the video attachment.

A. Experimental Setup

We implemented rock-and-walk manipulation in a range of settings, as shown in Fig. 8(a): Single- and dual-robot manipulation using UR10 arms and custom-made quadrotor aircraft. In the single-robot scenarios, the robot is equipped with a single-rigid-body end-effector for caging the object, similarly to the setting shown in Fig. 3(b). In the dual-robot scenarios, the robots interact with the object using cables, connecting the robot bodies and the object. The robots are all motion-controlled. The positioning accuracy of the arm and the quadrotor, which is important to the motion control tasks involved with rock and walk, is known to be up to ± 0.1 mm (according to the manufacturer) and measured to be up to ± 1 cm (according to our experiments with no external payload), respectively. We fabricated a range of oblique-circular-cone-shaped objects to be tested, which vary in size and material, as shown in Fig. 8(b). In the arm-based rock and walk, the state of the object is obtained by an inertial measurement unit (IMU) attached to the object. In the aerial rock and walk, a motion capture system is used for the state estimation of both the object and the quadrotors. Our software[3] takes as input the sensor data and runs the controllers in Section V-B, while synchronizing the motion of up to two robots.

B. Single-Arm Rock and Walk

We first tested rock-and-walk transport in a single-arm manipulation setting with a torus-shaped end-effector fixed to the wrist of the robot arm [top-left of Fig. 8(a)]. The end-effector has no internal mobility, but it is able to cage the object using the hole to accommodate the vertical rod of the object. The control point C is then the location of the end-effector on the vertical rod. Using the controllers, the robot first tips the object forward from an upright configuration, swings it up, and finally achieves a steady rock-and-walk gait for the object. Fig. 9(a) shows the steady-phase path traced by the ground contact point G on a lab floor over a span of 167 s during which the object walked approximately 1.4 m in the x-direction. As shown in Fig. 9(b),

[3][Online]. Available: https://github.com/HKUST-RML/rockwalk

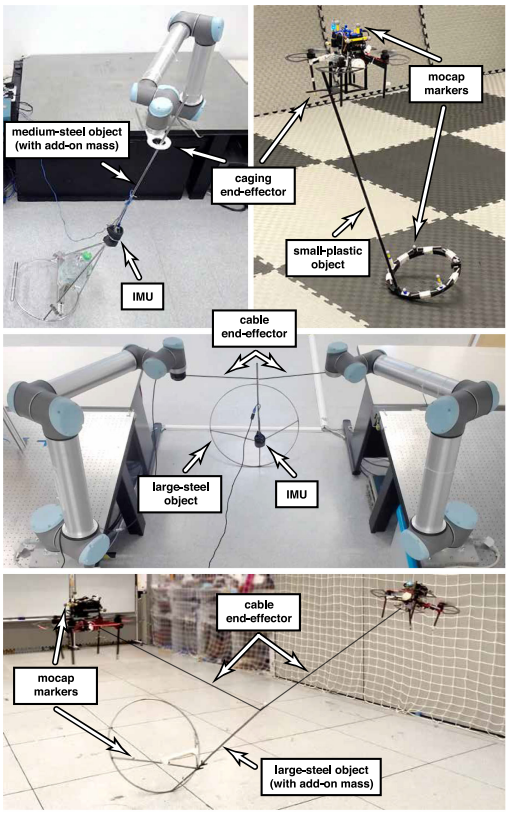

(a)

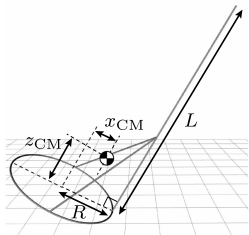

object (size-material)	mass (kg)	R (m)	L (m)	x_{CM} (m)	z_{CM} (m)
small-plastic	0.5	0.15	1.0	0.02	0.06
small-steel	1.0	0.15	1.5	0.09	0.40
medium-steel	1.4	0.23	1.5	0.11	0.36
medium-steel (with add-on mass)	8.5	0.23	1.5	0.07	0.23
large-steel	1.8	0.35	1.5	0.15	0.29
large-steel (with add-on mass)	2.6	0.35	1.5	0.15	0.37

(b)

Fig. 8. (a) Experiment settings: (top-left) one UR10 arm with a torus-shaped end-effector and (top-right) one quadrotor with a ∪-shaped end-effector; two UR10 arms (middle) and two quadrotors (bottom) for cable-driven rock-and-walk. (b) Specifications of the oblique-circular-cone-shaped objects used in our experiments [some shown in (a)].

the controller was able to keep the gait steady by effectively regulating the mechanical energy and the posture of the object.

The experiment was repeated on the lab floor under a range of conditions. The gait was stopped after the object walked a distance maximally up to 1.4 m due to the robot's limited workspace. The table in Fig. 9(c) summarizes the results. First, the first three rows of the table (small-, medium-, and large-steel at $\theta = 20.0^\circ$) show that a larger net forward distance per step is yielded when the circular base of the object is larger. This is because a larger base produces a longer stride (that is, the length of the integral curve of a step), given the same spinning amplitude. Second, a net forward distance per step is increased when the posture of the object is more upright, i.e., smaller θ (see the large-steel entries). This can be accounted for by the amount of energy loss in each step. We observe that when the object oscillates freely without running the controllers, the amount of energy loss decreases as θ becomes larger. Therefore, the energy controller commanded larger tilts when θ was smaller, and this gave rise to a larger net forward distance per step. In other words, greater forward strides result from increased energy expenditure. Third, the increased stride with a heavier object (compare the medium-steel entries) is also explained by the consideration of energy dissipation: The heavier object loses more energy when oscillating freely. We note that, the weight of the medium-steel object with an add-on mass exceeds the maximum payload of the manipulator arm.

On a treadmill [Fig. 10(a)], with no limit on walking distance, the robot was able to execute up to 1000 rock-and-walk steps and the object moved forward by up to approximately 15 m, on uphill and downhill slopes as well as on a level surface. The results of these experiments are recorded in the table in Fig. 10(b). In this long-range rock and walk, the errors in the object's heading direction can build up significantly, if uncontrolled, as can be seen in Fig. 9(a), where the errors in arm positioning or IMU sensing may have accounted for the object's trace straying slightly to the negative y-direction. The object on the treadmill was, therefore, steered occasionally to regulate its heading direction, as explained in Section V-B2, in a teleoperated manner by a human operator in case the object strays too close to the boundary of the treadmill track. The teleoperated steering can be made fully autonomous by means of global position feedback. In contrast to the experiments on the fixed floor, on the treadmill it is critical to be able to match the forward walking speed of the object with that of the treadmill. This was achieved by adding less energy to slow the object down when its posture becomes more upright (more energy added otherwise).

C. Single-Quadrotor Rock and Walk

Another instance of single-robot rock and walk was performed with a quadrotor using a zero-mobility, ∪-shaped end-effector fixed to the body [top-right of Fig. 8(a)]. The quadrotor manipulates the object by placing the vertical bar of the object in the concavity of the end-effector.

Fig. 11(a) and (b) presents a time-lapse sequence showing the quadrotor's takeoff, the initial forward tipping of the object, and a successful rock-and-walk gait. Here, the fluctuations in the values of the energy and configuration variables [Fig. 11(c)] were larger than those observed in the manipulator arm experiments. This difference can be accounted for by the quadrotor's poorer positioning accuracy and the softer terrain (foam mat) used. The table in Fig. 11(d) reports the results of aerial straight-line rock-and-walk transport repeated for different terrain conditions

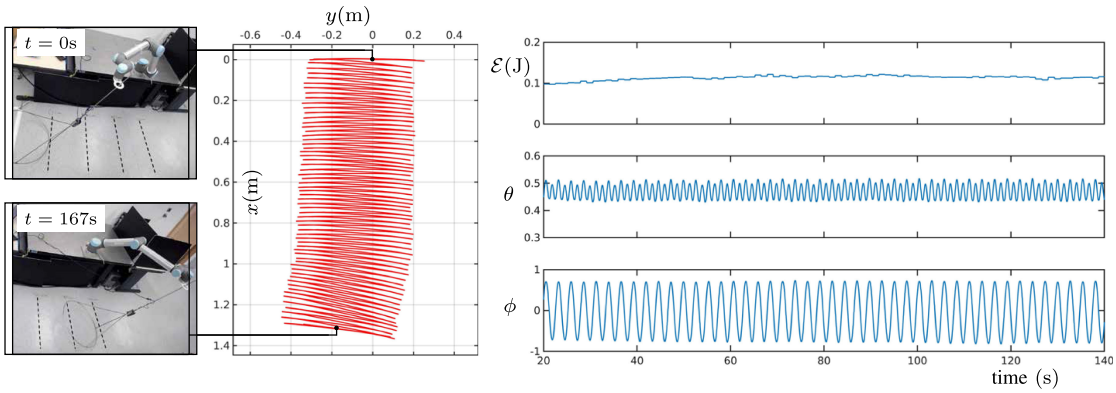

(a) (b)

Terrain	Slope	Object	Initial θ (°)	Net forward distance per step (cm)	Steps	Spinning amplitude (°)	Net forward distance (m)
lab floor	0%	small-steel	20.0	0.67	120	39.9 ± 4.0	0.80
		medium-steel	20.0	0.75	120	40.3 ± 2.1	0.90
		large-steel	20.0	1.07	120	39.5 ± 0.6	1.28
			25.0	0.93	140	37.7 ± 0.6	1.30
			30.0	0.84	160	36.9 ± 0.6	1.34
		medium-steel (with add-on mass)	20.0	2.17	60	40.1 ± 2.0	1.30

(c)

Fig. 9. Rock-and-walk by single-arm manipulation. (a) Path traced by G on the ground. (b) Time history of $\mathcal{E}$, the object's mechanical energy; θ, the nutation angle; and ϕ, the spin angle. (c) Results.

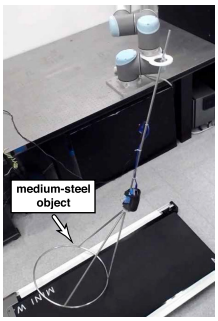

(a)

	Slope		
	0%	↘ 5%	↗ 5%
Net fwd. distance per step (cm)	1.44	1.49	1.42
Steps	1000	1000	620
Spinning amplitude (°)	40.4 ±3.1	44.6 ±3.3	39.3 ±2.9
Net forward distance (m)	14.4	14.9	8.8

(b)

Fig. 10. (a) Rock-and-walk on a treadmill. (b) Results.

and postures. The net forward distance per step on the foam-mat terrain was generally larger than that on the lab floor. This is because our controller commanded larger tilts on the foam mat in order to counter larger energy loss on the softer surface. The larger tilts in turn result in greater forward strides at a cost of increased energy expenditure, as also observed in the single-arm experiments. Another way to increase the net forward distance per step is to increase the amplitude of spinning: See the two lab floor experiments with $\theta = 35.0°$. In addition to the straight-line gaits reported in the table, Fig. 11(e) shows a circular rock-and-walk gait performed by constantly steering the object along a circle of radius 0.6 m.

D. Dual-Arm Rock and Walk

Next, rock-and-walk transport was performed in a dual-arm manipulation setting in which the wrist of each arm is connected to the object via cable [middle of Fig. 8(a)]. The common location on the object, where the two cables are fastened is then set to be the control point C. Two cables suffice to balance gravity and to tilt the object left and right for successive energy pumping-up and forward walking. The two arms are motion-controlled in a coordinated manner such that the aspect ratio of the $\vee$-shape formed by the cables is maintained. This will ensure that the control point C, at the vertex of the $\vee$-shape, is moved as desired.

Fig. 12 shows the results of two experiments in which the cables form an acute and an obtuse angle, respectively. The acute-angled cable configuration does not necessitate large cable tension forces, but the value of nutation θ needs to be sufficiently large to support the weight of the object. In contrast, the obtuse-angled configuration makes it possible to keep θ small although it requires large tensions. The table in Fig. 12 reports the results of the experiments. The obtuse-angled configuration outperformed in terms of the net forward distance due to the smaller nutation θ, as also observed in the single-robot experiments. However, the larger tensions that "fight against each other" in the obtuse-angled configuration, that is, large internal forces in the grasp of the object, rendered it harder to maintain the aspect ratio of the $\vee$-shape; this resulted in larger fluctuations in the nutation θ, compared with the acute-angled configuration (see the plots in Fig. 12).

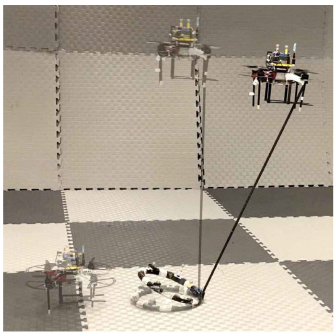

(a)

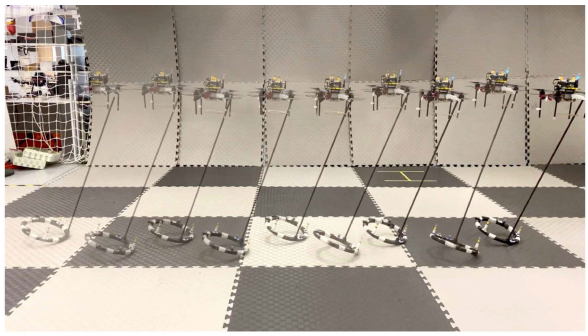

(b)

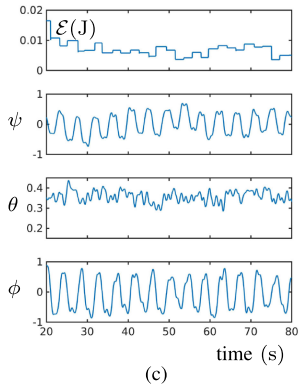

(c)

Object	Terrain	Initial θ (°)	Net forward distance per step (cm)	Steps	Spinning amplitude (°)	Net forward distance (m)
small-plastic	foam-mat	25.0	6.1	70	41.9 ± 7.6	4.27
		30.0	3.7	80	29.3 ± 7.9	2.94
		35.0	2.4	90	21.0 ± 7.6	2.18
	lab floor	30.0	1.4	100	41.7 ± 16.6	1.36
		35.0	1.2	100	41.2 ± 20.6	1.19
		35.0	2.3	100	55.0 ± 15.3	2.29
		40.0	0.8	100	31.3 ± 15.1	0.84

(d)

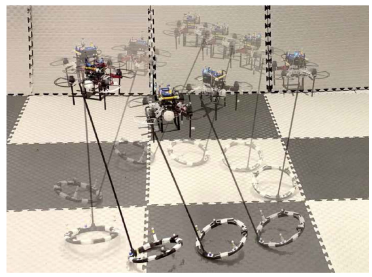

(e)

Fig. 11. Rock-and-walk by single-quadrotor manipulation. (a) The quadrotor takes off and tips the object forward. (b) Rock-and-walk gait across the foam-mat terrain. (c) Time history of the energy and the configuration of the object during the gait in (b). (d) Results of straight-line transport experiments. (e) Rock-and-walk along a circular path of diameter 1.2 m.

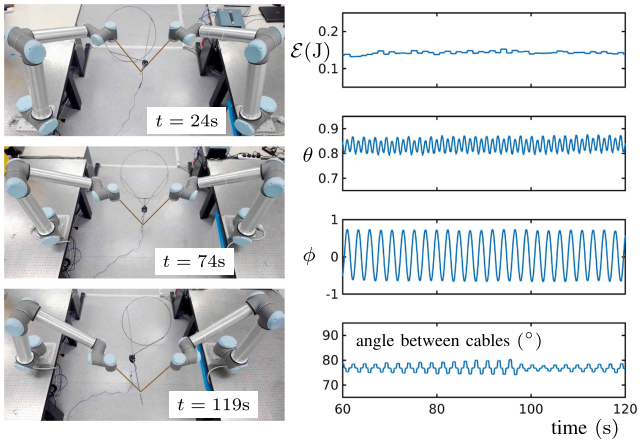

(a) (b)

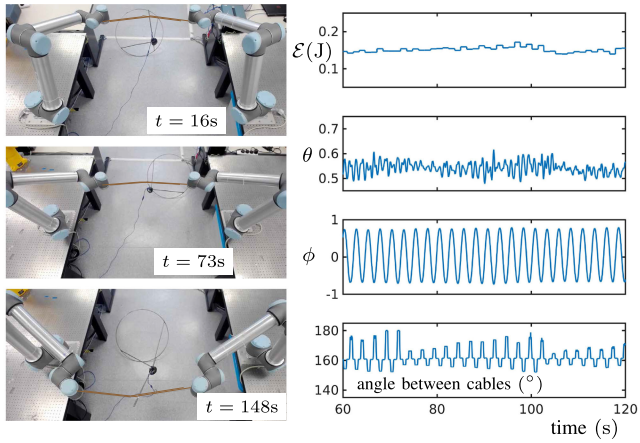

(c) (d)

Terrain	Object	Cable configuration	Angle between cables (°)	Initial θ (°)	Net forward distance per step (cm)	Steps	Spinning amplitude (°)	Net forward distance (m)
lab floor	large-steel	acute-angled	76.8	46.4	0.8	120	39.2 ± 0.6	0.98
		obtuse-angled	159.0	29.8	1.0	120	41.2 ± 1.0	1.20

(e)

Fig. 12. Rock-and-walk by dual-arm manipulation with two cables forming (a)–(b) an acute and (c)–(d) an obtuse angle. The progress of rock-and-walk is shown with the still photographs and the time plots of the energy and the configuration parameters. The table in (e) records the results of these experiments.

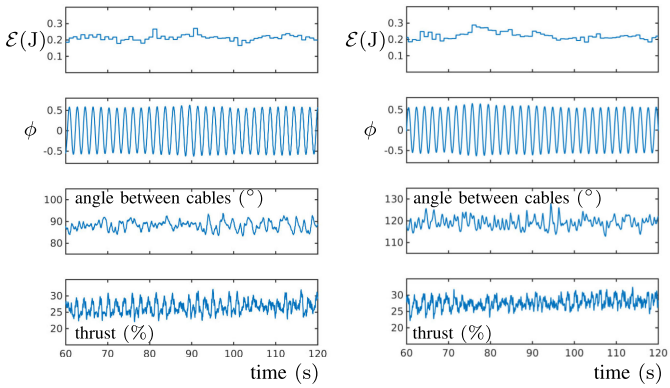

	Angle between cables (°)	
	90	120
Initial θ (°)	55	55
Steps	123	123
Net forward distance (m)	2.29	2.52
Net fwd. distance per step (cm)	1.86	2.05
Spinning amplitude (°)	34.0 ± 1.7	34.0 ± 2.8
Average thrust (%)	25.9	26.9

(c)

Fig. 13. Rock-and-walk by dual-quadrotor manipulation. The angle between the cables was set to be (a) 90° and (b) 120°. (c) Summary of the results.

E. Dual-Quadrotor Rock and Walk

Finally, dual-quadrotor rock and walk was performed using the same approach as the dual-arm experiment, by replacing the arms with quadrotors as a new motion control device [bottom of Fig. 8(a)]. The object used (large-steel with an add-on mass) weighs 2.6 kg, exceeding the maximum payload of the two quadrotors used.

Fig. 13 reports the results of two experiments, where the angles between the cables were set 90° and 120°, respectively. Despite the larger fluctuations in energy and configuration, as also observed in the single-quadrotor experiment, it was possible for the quadrotors to transport the object across the motion capture space. We note that, Fig. 13 features the time history of the quadrotor's thrust as a percentage. For reference, the value is around 100% when the quadrotor lifts up a 1-kg payload and 20% near the state of quasistatic hovering. The plot confirms the advantage of rock-and-walk transport that the robot only needs to support a fraction of the payload's weight.

F. Discussion

We conclude this section with a comparison of actual performance with theoretical prediction and a discussion of the range of application of rock and walk.

1) Theoretical Prediction Versus Actual Performance: Given the geometry of an object, it is possible to predict the actual performance of rock-and-walk transport. First, the trace of G during a step is obtained by the kinematics model (Section IV-B), and its arc length is determined by the amplitude of spinning. Second, the amount of the object's precession between steps is determined by the displacement of the control point C, shown as $\overline{C'_i C'_{i+1}}$ in Fig. 5. This is obtained from the required amount of a tilt (by rolling) to compensate for the discrepancy in G's position due to loss of energy. Lastly, the determined amount of precession leads to the estimation of net forward distance per step, as well as the fastest speed achievable using the dynamics model (Section IV-A). The fidelity of the prediction will depend on how accurately the energy loss can be determined.

a) Our experiment: For example, the net forward distances per step achieved by the large-steel object in the single-arm experiments reported in Fig. 9 are theoretically predicted to be 1.9 cm ($\theta = 20.0°$), 1.1 cm ($\theta = 25.0°$), and 0.8 cm ($\theta = 30.0°$); the actual values were 1.07, 0.93, and 0.84 cm, respectively. Here, the object was assumed to lose 3 to 5% of its energy per step, based on free oscillation experiments done with the object.

b) Moai: The moai demonstration [Fig. 1(a)] provides another example. We set up an oblique-cone-shaped object model that can approximate the 3-m-tall moai replica. Although the exact geometry of the replica is unknown, its dimensions were inferred to be $L = 3$ m, $R = 0.6$m, $x_{\mathrm{CM}} = 0.7$m, and $z_{\mathrm{CM}} = 1.5$m [see Fig. 8(b) for the notation], based on the information in [1]. If the amplitude of spinning and energy loss per step are assumed to be 20° (15°) and 15% (10%), the net forward distance per step was computed to be 4.1 cm (1.3 cm), when $\theta = 15°$. According to our dynamics model, the oscillation period of the object is 0.8 s. The forward speeds are then anticipated to be 10.3 and 3.3 cm/s, for the two cases, respectively. By comparison, the forward speed reported in [1] is 4.2 cm/s.

2) Range of Application: Based on the experiments reported, we discuss the range of application of rock and walk from three aspects: Object, robot, and terrain.

a) Object: Rock-and-walk transport is not merely limited to our objects contrived for the experiments, but the objects are required to have a close correspondence with the model in Fig. 2 and to exhibit the passive oscillatory dynamics as discussed in Section IV-C. Even if an object proves unsuitable for rock and walk, there is still a possibility of adjusting its geometric and mass properties for successful rock and walk, for example, by attaching additional masses because the robot system does not have to bear the entire weight of the object.

b) Robot: Beyond the single- and dual-robot implementation, three or more (groups of) robots, like the motivating example in Fig. 1(a), featuring three groups of experimenters, can be coordinated for rock-and-walk transport. For example, three (groups of) robots, each of which wields one cable, can be motion-controlled in a coordinated manner in such a way as to maintain the shape of the tetrahedron formed by the three cables. This is generalized from the dual-robot experiments, where the goal was to maintain the shape of the triangle formed by the two cables.

c) Terrain: Rock-and-walk transport requires a sufficiently smooth and frictional terrain in order to keep G rolling

without slipping. As shown in the treadmill experiments, rock and walk can be performed on a slope by taking advantage of the fact that the object is actually controlled to roll from side to side, i.e., Lie bracket motion, in the direction perpendicular to the direction of slope. The maximum allowable degree of sloping is expected to depend on the amount of energy loss per step. This is because the object will need to be steered more aggressively, and, thus, to be rolled on a steeper slope as the amount of energy loss increases.

VIII. Conclusion

A. Summary

This study presents the method of rock-and-walk manipulation that can be applied to the dynamic transport of large, heavy objects, for which conventional approaches based on prehensile grasping or quasistatic pushing can be unsuitable. Our results showed that the unsuitability of the conventional methods can be overcome by exploiting external resources such as contact with an environmental surface and the dynamics of the object, in conjunction with the robot's periodic efforts to regulate the energy and the posture of the object through feedback control. In terms of energy expenditure, the robot only needs to compensate for the energy loss mainly due to rolling resistance on the object, on a horizontal surface. The practicality and viability of our approach were demonstrated through the use of common robotic systems and a well-studied motion control scheme. However, we regard the scenario of object locomotion enabled by rock and walk as a special case that is limited to a certain class of objects, as also discussed.

B. Future Directions

Possible directions for future work include 1) the incorporation of a data-driven method for learning the physical parameters for rock and walk and for handling uncertainties and 2) outdoor demonstration of rock-and-walk transport in an end-to-end manner from object recognition to the performance of a successful gait, which will necessitate collaboration between heterogeneous robot platforms, for example, aerial and ground vehicles.

Appendix

We here present the kinetic energy T and the potential energy V of the object model, and the constraints $\mathbf{A}(\mathbf{q})$ on the model in full. Recall Fig. 2 for the object model.

A. Kinetic Energy T

First, ${}^s\mathbf{v}_{\mathrm{CM}}$, the velocity of the center of mass in the frame $\{s\}$, is expressed as follows in terms of ${}^s\mathbf{v}_D$, the velocity of D, the center of the disk:

$$\begin{aligned} {}^s\mathbf{v}_{\mathrm{CM}} &= {}^s\mathbf{v}_D + \frac{d}{dt}({}^b\mathbf{r}_{\mathrm{CM}|D}) \\ &= {}^s\mathbf{v}_D + {}^b\mathbf{v}_{\mathrm{CM}|D} + {}^s\boldsymbol{\omega}_b \times {}^b\mathbf{r}_{\mathrm{CM}|D} \end{aligned} \tag{10}$$

where

1) ${}^b\mathbf{r}_{\mathrm{CM}|D}$ is the position of the center of mass relative to D, expressed in the frame $\{b\}$

$${}^b\mathbf{r}_{\mathrm{CM}|D} = x_{\mathrm{CM}} c_\phi \hat{\mathbf{x}}_b + x_{\mathrm{CM}} s_\phi \hat{\mathbf{y}}_b + z_{\mathrm{CM}} \hat{\mathbf{z}}_b$$

x_{CM} and z_{CM} are the $\hat{\mathbf{x}}_b$- and $\hat{\mathbf{z}}_b$-coordinates of the center of mass when $\phi = 0$. Here, $\cos\phi$ and $\sin\phi$ are denoted by c_ϕ and s_ϕ for short, and similarly throughout the Appendix;

2) ${}^s\boldsymbol{\omega}_b$, the angular velocity of $\{b\}$ relative to $\{s\}$, is written as

$${}^s\boldsymbol{\omega}_b = \dot{\psi}\hat{\mathbf{z}}_s + \dot{\theta}\hat{\mathbf{y}}_b$$

3) ${}^b\mathbf{v}_{\mathrm{CM}|D}$, the velocity of the center of mass relative to D in $\{b\}$, is represented as

$${}^b\mathbf{v}_{\mathrm{CM}|D} = \dot{\phi}\hat{\mathbf{z}}_b \times {}^b\mathbf{r}_{\mathrm{CM}|D} = -x_{\mathrm{CM}}\dot{\phi} s_\phi \hat{\mathbf{x}}_b + x_{\mathrm{CM}}\dot{\phi} c_\phi \hat{\mathbf{y}}_b.$$

Considering the relationship between $\{s\}$ and $\{b\}$

$$\begin{aligned} \hat{\mathbf{x}}_b &= -s_\psi c_\theta \hat{\mathbf{x}}_s + c_\psi c_\theta \hat{\mathbf{y}}_s - s_\theta \hat{\mathbf{z}}_s \\ \hat{\mathbf{y}}_b &= -c_\psi \hat{\mathbf{x}}_s - s_\psi \hat{\mathbf{y}}_s \\ \hat{\mathbf{z}}_b &= -s_\psi s_\theta \hat{\mathbf{x}}_s + c_\psi s_\theta \hat{\mathbf{y}}_s + c_\theta \hat{\mathbf{z}}_s \end{aligned} \tag{11}$$

${}^s\mathbf{v}_{\mathrm{CM}} = [{}^s v^x_{\mathrm{CM}}, {}^s v^y_{\mathrm{CM}}, {}^s v^z_{\mathrm{CM}}]^T$ is written as

$$\begin{aligned} {}^s v^x_{\mathrm{CM}} =\ & \dot{x}_D + (x_{\mathrm{CM}}\, s_\psi\, s_\phi - z_{\mathrm{CM}}\, c_\psi\, s_\theta - x_{\mathrm{CM}}\, c_\psi\, c_\theta\, c_\phi)\,\dot{\psi} \\ & - (z_{\mathrm{CM}}\, s_\psi\, c_\theta - x_{\mathrm{CM}}\, s_\psi\, c_\phi\, s_\theta)\,\dot{\theta} \\ & + (x_{\mathrm{CM}}\, c_\theta\, s_\psi\, s_\phi - x_{\mathrm{CM}}\, c_\psi\, c_\phi)\,\dot{\phi} \\ {}^s v^y_{\mathrm{CM}} =\ & \dot{y}_D - (x_{\mathrm{CM}}\, c_\psi\, s_\phi + z_{\mathrm{CM}}\, s_\psi\, s_\theta + x_{\mathrm{CM}}\, c_\theta\, c_\phi\, s_\psi)\,\dot{\psi} \\ & + (z_{\mathrm{CM}}\, c_\psi\, c_\theta - x_{\mathrm{CM}}\, c_\phi\, c_\psi\, s_\theta)\,\dot{\theta} \\ & - (x_{\mathrm{CM}}\, c_\phi\, s_\psi + x_{\mathrm{CM}}\, c_\psi\, c_\theta\, s_\phi)\,\dot{\phi} \\ {}^s v^z_{\mathrm{CM}} =\ & (R\, c_\theta - z_{\mathrm{CM}}\, s_\theta - x_{\mathrm{CM}}\, c_\theta\, c_\phi)\,\dot{\theta} + (x_{\mathrm{CM}}\, s_\theta\, s_\phi)\,\dot{\phi}. \end{aligned} \tag{12}$$

Note, R denotes the radius of the base disk and the relationship $z_D = R s_\theta$ was substituted into ${}^s v^z_{\mathrm{CM}}$.

${}^s\mathbf{v}_{\mathrm{CM}}$ then leads to the kinetic energy T of the object model

$$T = \frac{1}{2} m\, {}^s\mathbf{v}_{\mathrm{CM}} \cdot {}^s\mathbf{v}_{\mathrm{CM}} \tag{13}$$

where m is the mass of the object. In full

$$\begin{aligned} T = \frac{1}{2} m \Big(& R^2\,\dot{\theta}^2\, {c_\theta}^2 - 2\,R\,\dot{\theta}^2\, x_{\mathrm{CM}}\, {c_\theta}^2\, c_\phi - s_{2\theta}\, R\,\dot{\theta}^2\, z_{\mathrm{CM}} \\ & + 2\, s_\theta\, s_\phi\, R\,\dot{\theta}\,\dot{\phi}\, x_{\mathrm{CM}}\, c_\theta + \dot{x}_D^2 - 2\, c_\psi\, \dot{x}_D\,\dot{\psi}\, x_{\mathrm{CM}}\, c_\theta\, c_\phi \\ & + 2\, s_\psi\, s_\phi\, \dot{x}_D\,\dot{\psi}\, x_{\mathrm{CM}} - 2\, c_\psi\, s_\theta\, \dot{x}_D\,\dot{\psi}\, z_{\mathrm{CM}} \\ & + 2\, s_\psi\, s_\theta\, \dot{x}_D\,\dot{\theta}\, x_{\mathrm{CM}}\, c_\phi - 2\, s_\psi\, \dot{x}_D\,\dot{\theta}\, z_{\mathrm{CM}}\, c_\theta \\ & + 2\, s_\psi\, s_\phi\, \dot{x}_D\,\dot{\phi}\, x_{\mathrm{CM}}\, c_\theta - 2\, c_\psi\, \dot{x}_D\,\dot{\phi}\, x_{\mathrm{CM}}\, c_\phi + \dot{y}_D^2 \\ & - 2\, s_\psi\, \dot{y}_D\,\dot{\psi}\, x_{\mathrm{CM}}\, c_\theta\, c_\phi - 2\, c_\psi\, s_\phi\, \dot{y}_D\,\dot{\psi}\, x_{\mathrm{CM}} \\ & - 2\, s_\psi\, s_\theta\, \dot{y}_D\,\dot{\psi}\, z_{\mathrm{CM}} - 2\, c_\psi\, s_\theta\, \dot{y}_D\,\dot{\theta}\, x_{\mathrm{CM}}\, c_\phi \end{aligned}$$

$$
\begin{aligned}
&+ 2\,c_\psi\,\dot{y}_D\,\dot{\theta}\,z_{\mathrm{CM}}\,c_\theta - 2\,c_\psi\,s_\phi\,\dot{y}_D\,\dot{\phi}\,x_{\mathrm{CM}}\,c_\theta \\
&- 2\,s_\psi\,\dot{y}_D\,\dot{\phi}\,x_{\mathrm{CM}}\,c_\phi + \dot{\psi}^2\,{x_{\mathrm{CM}}}^2\,{c_\theta}^2\,{c_\phi}^2 - \dot{\psi}^2\,{x_{\mathrm{CM}}}^2\,{c_\phi}^2 \\
&+ \dot{\psi}^2\,{x_{\mathrm{CM}}}^2 + 2\,s_\theta\,\dot{\psi}^2\,x_{\mathrm{CM}}\,z_{\mathrm{CM}}\,c_\theta\,c_\phi - \dot{\psi}^2\,{z_{\mathrm{CM}}}^2\,{c_\theta}^2 \\
&+ \dot{\psi}^2\,{z_{\mathrm{CM}}}^2 + 2\,s_\theta\,s_\phi\,\dot{\psi}\,\dot{\theta}\,{x_{\mathrm{CM}}}^2\,c_\phi - 2\,s_\phi\,\dot{\psi}\,\dot{\theta}\,x_{\mathrm{CM}}\,z_{\mathrm{CM}}\,c_\theta \\
&+ 2\,\dot{\psi}\,\dot{\phi}\,{x_{\mathrm{CM}}}^2\,c_\theta + 2\,s_\theta\,\dot{\psi}\,\dot{\phi}\,x_{\mathrm{CM}}\,z_{\mathrm{CM}}\,c_\phi + \dot{\theta}^2\,{x_{\mathrm{CM}}}^2\,{c_\phi}^2 \\
&+ \dot{\theta}^2\,{z_{\mathrm{CM}}}^2 - 2\,s_\phi\,\dot{\theta}\,\dot{\phi}\,x_{\mathrm{CM}}\,z_{\mathrm{CM}} + \dot{\phi}^2\,{x_{\mathrm{CM}}}^2\Big). \qquad (14)
\end{aligned}
$$

B. Potential Energy V

The potential energy V is written in terms of the $\hat{\mathbf{z}}_s$-coordinate of the center of mass

$$
\begin{aligned}
V &= m\,g\,\left({}^s\mathbf{r}_D + {}^b\mathbf{r}_{\mathrm{CM}|D}\right)\cdot\hat{\mathbf{z}}_s \\
&= m\,g\,\left(R\,s_\theta + z_{\mathrm{CM}}\,c_\theta - x_{\mathrm{CM}}\,c_\phi\,s_\theta\right) \qquad (15)
\end{aligned}
$$

where g denotes the gravitational acceleration pointing in the negative $\hat{\mathbf{z}}_s$-direction.

C. Pfaffian Constraint Matrix $\mathbf{A}(\mathbf{q})$

${}^s\mathbf{v}_G = [{}^s v_G^x \quad {}^s v_G^y]^T$, the velocity of the ground contact point G, is expressed in terms of the generalized coordinates $\mathbf{q} = (q_1, q_2, q_3, q_4, q_5) = (x_D, y_D, \psi, \theta, \phi)$ as follows:

$$
\begin{aligned}
{}^s v_G^x &= \dot{x}_D - R\,\dot{\psi}\,c_\psi\,c_\theta + R\,\dot{\theta}\,s_\psi\,s_\theta - R\,\dot{\phi}\,c_\psi \\
{}^s v_G^y &= \dot{y}_D - R\,\dot{\psi}\,c_\theta\,s_\psi - R\,\dot{\theta}\,c_\psi\,s_\theta - R\,\dot{\phi}\,s_\psi. \qquad (16)
\end{aligned}
$$

The $\hat{\mathbf{x}}_s$- and $\hat{\mathbf{y}}_s$-components of ${}^s\mathbf{v}_C$, the velocity of the control point C which is assumed at the tip of the vertical bar of the object model shown in Fig. 8, is similarly given by

$$
\begin{aligned}
{}^s v_C^x = {}& \dot{x}_D + \left(R\,s_\psi\,s_\phi - L\,c_\psi\,s_\theta - R\,c_\psi\,c_\theta\,c_\phi\right)\dot{\psi} \\
&- \left(L\,s_\psi\,c_\theta - R\,s_\psi\,c_\phi\,s_\theta\right)\dot{\theta} \\
&+ \left(R\,c_\theta\,s_\psi\,s_\phi - R\,c_\psi\,c_\phi\right)\dot{\phi} \\
{}^s v_C^y = {}& \dot{y}_D - \left(R\,c_\psi\,s_\phi + L\,s_\psi\,s_\theta + R\,c_\theta\,c_\phi\,s_\psi\right)\dot{\psi} \\
&+ \left(L\,c_\psi\,c_\theta - R\,c_\phi\,c_\psi\,s_\theta\right)\dot{\theta} \\
&- \left(R\,c_\phi\,s_\psi + R\,c_\psi\,c_\theta\,s_\phi\right)\dot{\phi}. \qquad (17)
\end{aligned}
$$

Note that, the $\hat{\mathbf{z}}_s$-component of ${}^s\mathbf{v}_C$ is dependent on the other components.

The matrix $\mathbf{A}(\mathbf{q}) \in \mathbb{R}^{4\times 5}$ is then obtained by putting together the coefficients of the expressions above

$$
\mathbf{A}(\mathbf{q}) = \begin{pmatrix} a_{11} & a_{12} & a_{13} & a_{14} & a_{15} \\ a_{21} & a_{22} & a_{23} & a_{24} & a_{25} \\ a_{31} & a_{32} & a_{33} & a_{34} & a_{35} \\ a_{41} & a_{42} & a_{43} & a_{44} & a_{45} \end{pmatrix} \qquad (18)
$$

where

$$
\begin{aligned}
&a_{11} = 1, \quad a_{12} = 0, \quad a_{13} = -R\,c_\psi\,c_\theta, \quad a_{14} = R\,s_\psi\,s_\theta, \\
&a_{15} = -R\,c_\psi \\
&a_{21} = 0, \quad a_{22} = 1, \quad a_{23} = -R\,c_\theta\,s_\psi, \quad a_{24} = -R\,c_\psi\,s_\theta, \\
&a_{25} = -R\,s_\psi \\
&a_{31} = 1, \quad a_{32} = 0, \quad a_{33} = R\,s_\psi\,s_\phi - L\,c_\psi\,s_\theta - R\,c_\psi\,c_\theta\,c_\phi, \\
&a_{34} = R\,s_\psi\,c_\phi\,s_\theta - L\,s_\psi\,c_\theta, \quad a_{35} = R\,c_\theta\,s_\psi\,s_\phi - R\,c_\psi\,c_\phi \\
&a_{41} = 0, \quad a_{42} = 1, \quad a_{43} = -R\,c_\psi\,s_\phi - L\,s_\psi\,s_\theta - R\,c_\theta\,c_\phi\,s_\psi, \\
&a_{44} = L\,c_\psi\,c_\theta - R\,c_\phi\,c_\psi\,s_\theta, \quad a_{45} = -R\,c_\phi\,s_\psi - R\,c_\psi\,c_\theta\,s_\phi.
\end{aligned}
$$

REFERENCES

[1] C. P. Lipo, T. L. Hunt, and S. R. Haoa, "The 'walking' megalithic statues (moai) of Easter Island," *J. Archaeological Sci.*, vol. 40, no. 6, pp. 2859–2866, 2013.

[2] A. Nazir and J. Seo, "Passive dynamic object locomotion by rocking and walking manipulation," in *Proc. Int. Conf. Robot. Automat.*, 2019, pp. 7926–7932.

[3] M. A. Erdmann and M. T. Mason, "An exploration of sensorless manipulation," *IEEE J. Robot. Autom.*, vol. 4, no. 4, pp. 369–379, Aug. 1988.

[4] A. A. Rizzi and D. E. Koditschek, "Progress in spatial robot juggling," in *Proc. IEEE Int. Conf. Robot. Automat.*, vol. 1, 1992, pp. 775–780.

[5] K. M. Lynch and M. T. Mason, "Dynamic nonprehensile manipulation: Controllability, planning, and experiments," *Int. J. Robot. Res.*, vol. 18, no. 1, pp. 64–92, 1999.

[6] P. Donner and M. Buss, "Cooperative swinging of complex pendulum-like objects: Experimental evaluation," *IEEE Trans. Robot.*, vol. 32, no. 3, pp. 744–753, Jun. 2016.

[7] J. Shi, J. Z. Woodruff, P. B. Umbanhowar, and K. M. Lynch, "Dynamic in-hand sliding manipulation," *IEEE Trans. Robot.*, vol. 33, no. 4, pp. 778–795, Aug. 2017.

[8] A. Zeng, S. Song, J. Lee, A. Rodriguez, and T. Funkhouser, "TossingBot: Learning to throw arbitrary objects with residual physics," *IEEE Trans. Robot.*, vol. 36, no. 4, pp. 1307–1319, Aug. 2020.

[9] L. U. Odhner *et al.*, "A compliant, underactuated hand for robust manipulation," *Int. J. Robot. Res.*, vol. 33, no. 5, pp. 736–752, 2014.

[10] J. Sastra, S. Chitta, and M. Yim, "Dynamic rolling for a modular loop robot," *Int. J. Robot. Res.*, vol. 28, no. 6, pp. 758–773, 2009.

[11] R. Balasubramanian, A. A. Rizzi, and M. T. Mason, "Legless locomotion: A novel locomotion technique for legged robots," *Int. J. Robot. Res.*, vol. 27, no. 5, pp. 575–594, 2008.

[12] T. McGeer, "Passive dynamic walking," *Int. J. Robot. Res.*, vol. 9, no. 2, pp. 62–82, 1990.

[13] M. J. Coleman, M. Garcia, K. Mombaur, and A. Ruina, "Prediction of stable walking for a toy that cannot stand," *Phys. Rev. E*, vol. 64, no. 2, 2001, Art. no. 022901.

[14] S. H. Collins, M. Wisse, and A. Ruina, "A three-dimensional passive-dynamic walking robot with two legs and knees," *Int. J. Robot. Res.*, vol. 20, no. 7, pp. 607–615, 2001.

[15] R. Tedrake, T. W. Zhang, M.-F. Fong, and H. S. Seung, "Actuating a simple 3D passive dynamic walker," in *Proc. IEEE Int. Conf. Robot. Automat.*, 2004, pp. 4656–4661.

[16] P. Steinkamp, "A statically unstable passive Hopper: Design evolution," *J. Mechanisms Robot.*, vol. 9, no. 1, 2017, Art. no. 011016.

[17] M. T. Mason, *Mechanics of Robotic Manipulation*. Cambridge, MA, USA: MIT Press, Aug. 2001.

[18] A. Bicchi, "Hands for dexterous manipulation and robust grasping: A difficult road toward simplicity," *IEEE Trans. Robot. Automat.*, vol. 16, no. 6, pp. 652–662, Dec. 2000.

[19] V. Babin and C. Gosselin, "Picking, grasping, or scooping small objects lying on flat surfaces: A design approach," *Int. J. Robot. Res.*, vol. 37, no. 12, pp. 1484–1499, 2018.

[20] T. He, S. Aslam, Z. Tong, and J. Seo, "Scooping manipulation via motion control with a two-fingered gripper and its application to bin picking," *IEEE Robot. Automat. Lett.*, vol. 6, no. 4, pp. 6394–6401, Oct. 2021.

[21] Z. Tong, Y. H. Ng, C. H. Kim, T. He, and J. Seo, "Dig-grasping via direct quasistatic interaction using asymmetric fingers: An approach to effective bin picking," *IEEE Robot. Automat. Lett.*, vol. 6, no. 2, pp. 3033–3040, Apr. 2021.
[22] M. T. Mason, "Mechanics and planning of manipulator pushing operations," *Int. J. Robot. Res.*, vol. 5, no. 3, pp. 53–71, 1986.
[23] K. M. Lynch and M. T. Mason, "Stable pushing: Mechanics, controllability, and planning," *Int. J. Robot. Res.*, vol. 15, no. 6, pp. 533–556, 1996.
[24] N. Chavan-Dafle, R. Holladay, and A. Rodriguez, "Planar in-hand manipulation via motion cones," *Int. J. Robot. Res.*, vol. 39, no. 2/3, pp. 163–182, 2020.
[25] M. Bauza and A. Rodriguez, "A probabilistic data-driven model for planar pushing," in *Proc. IEEE Int. Conf. Robot. Automat.*, 2017, pp. 3008–3015.
[26] M. T. Mason, D. K. Pai, D. Rus, J. Howell, L. R. Taylor, and M. A. Erdmann, "Experiments with desktop mobile manipulators," in *Experimental Robotics VI*. London, U.K.: Springer, 2000, pp. 37–46.
[27] A. Specian, C. Mucchiani, M. Yim, and J. Seo, "Robotic edge-rolling manipulation: A grasp planning approach," *IEEE Robot. Automat. Lett.*, vol. 3, no. 4, pp. 3137–3144, Oct. 2018.
[28] Y. Aiyama, M. Inaba, and H. Inoue, "Pivoting: A new method of graspless manipulation of object by robot fingers," in *Proc. IEEE/RSJ Int. Conf. Intell. Robots Syst.*, 1993, pp. 136–143.
[29] E. Yoshida, M. Poirier, J.-P. Laumond, R. Alami, and K. Yokoi, "Pivoting based manipulation by humanoids: A controllability analysis," in *Proc. IEEE/RSJ Int. Conf. Intell. Robots Syst.*, 2007, pp. 1130–1135.
[30] F. Shi, M. Zhao, M. Murooka, K. Okada, and M. Inaba, "Aerial regrasping: Pivoting with transformable multilink aerial robot," in *Proc. IEEE Int. Conf. Robot. Automat.*, 2020, pp. 200–207.
[31] M. T. Mason, "Progress in nonprehensile manipulation," *Int. J. Robot. Res.*, vol. 18, no. 11, pp. 1129–1141, Nov. 1999.
[32] S. Makita and W. Wan, "A survey of robotic caging and its applications," *Adv. Robot.*, vol. 31, no. 19/20, pp. 1071–1085, 2017.
[33] A. Shirizly, E. D. Rimon, and W. Wan, "Contact space computation of two-finger gravity based caging grasps security measure," *IEEE Robot. Automat. Lett.*, vol. 6, no. 2, pp. 572–579, 2021.
[34] C. Davidson and A. Blake, "Error-tolerant visual planning of planar grasp," in *Proc. 6th Int. Conf. Comput. Vis.*, 1998, pp. 911–916.
[35] A. Rodriguez, M. T. Mason, and S. Ferry, "From caging to grasping," *Int. J. Robot. Res.*, vol. 31, no. 7, pp. 886–900, 2012.
[36] J. Seo, M. Yim, and V. Kumar, "A theory on grasping objects using effectors with curved contact surfaces and its application to whole-arm grasping," *Int. J. Robot. Res.*, vol. 35, no. 9, pp. 1080–1102, 2016.
[37] R. R. Ma, W. G. Bircher, and A. M. Dollar, "Modeling and evaluation of robust whole-hand caging manipulation," *IEEE Trans. Robot.*, vol. 35, no. 3, pp. 549–563, Jun. 2019.
[38] G. A. S. Pereira, M. F. M. Campos, and V. Kumar, "Decentralized algorithms for multi-robot manipulation via caging," *Int. J. Robot. Res.*, vol. 23, no. 7/8, pp. 783–795, 2004.
[39] W. Wan, B. Shi, Z. Wang, and R. Fukui, "Multirobot object transport via robust caging," *IEEE Trans. Syst. Man Cybern. Syst.*, vol. 50, no. 1, pp. 270–280, Jan. 2020.
[40] J. Albus, R. Bostelman, and N. Dagalakis, "The NIST robocrane," *J. Robotic Syst.*, vol. 10, no. 5, pp. 709–724, 1993.
[41] H. Arisumi, K. Yokoi, and K. Komoriya, "Casting manipulation—Midair control of a gripper by impulsive force," *IEEE Trans. Robot.*, vol. 24, no. 2, pp. 402–415, Apr. 2008.
[42] X. Jiang, E. Barnett, and C. Gosselin, "Dynamic point-to-point trajectory planning beyond the static workspace for six-DOF cable-suspended parallel robots," *IEEE Trans. Robot.*, vol. 34, no. 3, pp. 781–793, Jun. 2018.
[43] J. Fink, N. Michael, S. Kim, and V. Kumar, "Planning and control for cooperative manipulation and transportation with aerial robots," *Int. J. Robot. Res.*, vol. 30, no. 3, pp. 324–334, 2011.
[44] K. Sreenath, N. Michael, and V. Kumar, "Trajectory generation and control of a quadrotor with a cable-suspended load—A differentially-flat hybrid system," in *Proc. IEEE Int. Conf. Robot. Automat.*, 2013, pp. 4888–4895.
[45] B. E. Jackson, T. A. Howell, K. Shah, M. Schwager, and Z. Manchester, "Scalable cooperative transport of cable-suspended loads with UAVs using distributed trajectory optimization," *IEEE Robot. Automat. Lett.*, vol. 5, no. 2, pp. 3368–3374, Apr. 2020.
[46] J. H. Ginsberg, *Advanced Engineering Dynamics*. Cambridge, U.K.: Cambridge Univ. Press, 1998.
[47] A. M. Bloch, "Nonholonomic mechanics," in *Nonholonomic Mechanics and Control*. New York, NY, USA: Springer, 2003, pp. 207–276.
[48] C. C. Chung and J. Hauser, "Nonlinear control of a swinging pendulum," *Automatica*, vol. 31, no. 6, pp. 851–862, 1995.
[49] M. W. Spong, "The swing up control problem for the acrobot," *IEEE control Syst. Mag.*, vol. 15, no. 1, pp. 49–55, Feb. 1995.
[50] M. H. Raibert, *Legged Robots That Balance*. Cambridge, MA, USA: MIT press, 1986.

Abdullah Nazir received the B.Eng. degree in mechanical engineering from the the University of Hong Kong, Hong Kong, in 2017, and the Ph.D. degree in electronic and computer engineering from the Hong Kong University of Science and Technology, Hong Kong, in 2021.

He is currently a Postdoctoral Fellow with the Hong Kong Centre of Logistics Robotics, Hong Kong, and the Chinese University of Hong Kong, Hong Kong. His research interests include developing learning algorithms that enable intelligent grasping and manipulation.

Pu Xu received the B.Eng. degree in computer science and technology from Hunan Normal University, Changsha, China, in 2014, and the M.Phil. degree from the Hong Kong University of Science and Technology (HKUST), Hong Kong, in 2021.

He is currently a Research Assistant with the Department of Mechanical and Aerospace Engineering, HKUST. His research interests include manipulation and locomotion.

Jungwon Seo (Member, IEEE) received the Ph.D. degree in mechanical engineering and applied mechanics from the General Robotics, Automation, Sensing and Perception Laboratory, University of Pennsylvania, Philadelphia, PA, USA, in 2014.

He is an Assistant Professor of Mechanical and Aerospace/Electronic and Computer Engineering with the Hong Kong University of Science and Technology, Hong Kong. His research interests include grasping and manipulation.

Dr. Seo was the recipient of the IEEE International Conference on Robotics and Automation (ICRA) 2019 Best Paper Award in Robot Manipulation and IEEE ICRA 2014 Best Paper Award in Automation.